

Topological Hall effect and magnetic states in the Nowotny chimney ladder compound Cr₁₁Ge₁₉Yu Li ^{1,*}, Xin Gui,² Mojammel A. Khan ^{1,3}, Weiwei Xie,² David P. Young,¹ and J. F. DiTusa^{1,†}¹*Department of Physics & Astronomy, Louisiana State University, Baton Rouge, Louisiana 70803, USA*²*Department of Chemistry, Louisiana State University, Baton Rouge, Louisiana 70803, USA*³*Department of Physics and Astronomy and Department of Chemistry, Johns Hopkins University, Baltimore, Maryland 21210, USA*

(Received 9 October 2020; revised 9 December 2020; accepted 7 January 2021; published 27 January 2021)

We have investigated the magnetic and charge transport properties of single crystals of the Nowotny chimney ladder compound Cr₁₁Ge₁₉ and mapped out a comprehensive phase diagram reflecting the complicated interplay between the Dzyaloshinskii-Moriya (DM) interaction, the dipolar interaction, and the magnetic anisotropy. We have identified a set of interesting magnetic phases and attributed a finite topological Hall effect to the recently discovered biskyrmion phase. These data also suggest the existence of an antiskyrmion state at finite fields for temperatures just below the magnetic ordering temperature T_c as indicated by a distinct change in sign of the topological Hall effect. Above T_c , we discovered a region of enhanced magnetic response corresponding to a disordered phase likely existing near the ferromagnetic critical point under small magnetic fields. Strong spin chirality fluctuations are demonstrated by the large value of the topological Hall resistivity persisting up to 1 T, which is most likely due to the existence of the DM interaction. We argue that changes to the topological Hall effect correspond to different topological spin textures that are controlled by magnetic dipolar and DM interactions that vary in importance with temperature.

DOI: [10.1103/PhysRevB.103.024445](https://doi.org/10.1103/PhysRevB.103.024445)**I. INTRODUCTION**

Skyrmions and antiskyrmions are nanoscale particlelike spin textures found in a variety of systems from chiral structured magnets to thin ferromagnetic films [1–3]. Each skyrmion or antiskyrmion carries a positive or negative topological charge known as the scalar spin chirality. When a skyrmion meets an antiskyrmion, they are expected to annihilate and emit magnons [4], in analogy to the annihilation of matter and antimatter generating electromagnetic radiation. These topological magnetic spin textures possess a net scalar spin chirality which is implicitly determined by the crystal structure and dominant magnetic interactions. For instance, skyrmion phases in chiral magnets are caused by the isotropic Dzyaloshinskii-Moriya (DM) interaction [5,6], while antiskyrmions found in some Heusler alloys are due to an anisotropic DM interaction with opposite signs along the x and y axes [7,8] that is favored by the D_{2d} crystal symmetry. Moreover, in many centrosymmetric magnets in the absence of the DM interaction, the interplay between the dipolar interaction and the magnetic anisotropy leads to the formation of biskyrmions, a bound pair of skyrmions with opposite helicity [9–12]. In principle, one could tune the anisotropic DM interaction with respect to the dipolar energies and magnetic anisotropies to create a transition between skyrmion states and antiskyrmion states. Recently, it was reported [13,14] that a topological transformation from antiskyrmions to skyrmions

occurs in noncentrosymmetric Mn_{1.4}Pt_{0.9}Pd_{0.1}Sn, making the D_{2d} systems especially interesting.

Among the few topological magnetic materials known, Cr₁₁Ge₁₉ is unique as it is the first noncentrosymmetric compound found to host a biskyrmion spin texture [15]. Its crystal structure contains fourfold helices of Ge nested inside [Figs. 1(a) and 1(b)]. Cr₁₁Ge₁₉ is one of the two known members of the Nowotny chimney ladder compounds [16,17] to display a magnetically ordered ground state. Its crystal structure has the D_{2d} symmetry thought to support an antisymmetric DM interaction favoring antiskyrmion formation, as is the case in the tetragonal Heusler compound Mn_{1.4}Pt_{0.9}Pd_{0.1}Sn [7]. In contrast to the expectation of antiskyrmions, only biskyrmions were reported in a recent Lorentz transmission electron microscopy (LTEM) experiment performed on a thin lamella at 6 K and a field of 40 mT, suggesting the dominance of dipolar interactions [15]. Generally, the magnetic dipolar interaction is long ranged and can be screened by spin fluctuations as the system approaches the magnetic transition temperature, while the DM interaction is thought to be temperature independent. This provides an opportunity to tune the strength of the relevant interactions with temperature and sample geometry in anticipation of a topological phase of antiskyrmions in Cr₁₁Ge₁₉ when the DM interaction is dominant.

In this paper, we report an extensive investigation of the magnetic and charge transport properties of high-quality Cr₁₁Ge₁₉ single crystals. We have mapped out a comprehensive phase diagram and indicate a set of interesting magnetic phases in Cr₁₁Ge₁₉ that are dependent on temperature and field. These data suggest that the recently discovered biskyrmion phase [15] of this material is just one of several

*yuli1@lsu.edu

†ditusa@phys.lsu.edu

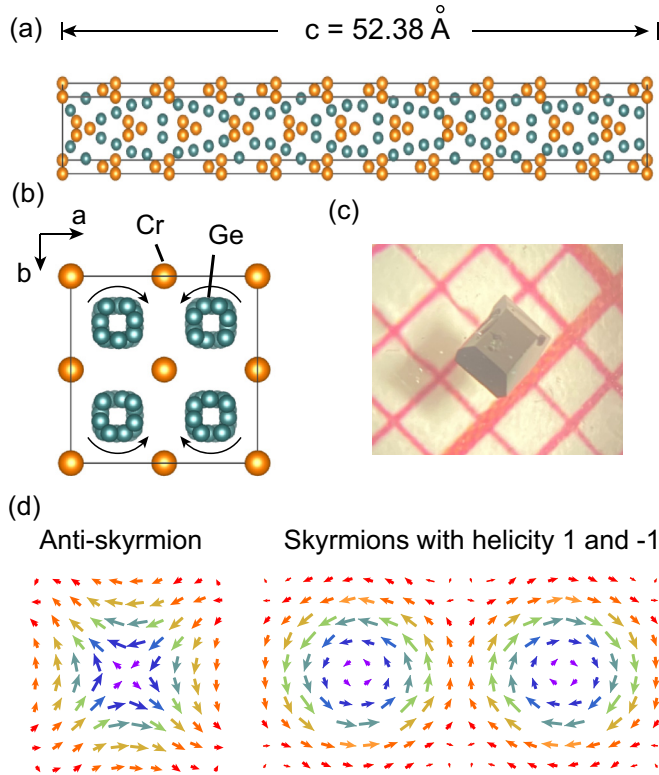


FIG. 1. Crystal structure, morphology, and skyrmion schematics. Crystal structure of $\text{Cr}_{11}\text{Ge}_{19}$ (a) along the c axis and (b) in the ab plane. Orange (blue) spheres are Cr (Ge) atoms. The arrows represent the direction of rotation of the Ge helices. The surrounding Cr helices have the opposite sense of rotation. (c) Picture of a $\text{Cr}_{11}\text{Ge}_{19}$ crystal. The box size on the graph paper is $1 \times 1 \text{ mm}^2$. (d) In-plane spin configuration of an antiskyrmion and a biskyrmion pair. The red color represents spin up, while purple color corresponds to spin down.

interesting magnetic phases. A tendency for the redistribution of spin textures towards the stripe ordered state is suggested at low temperatures, while a strongly fluctuating phase (or region) at small magnetic fields and above the magnetic ordering temperature is indicated by the magnetic susceptibility. Based on measurements of the topological Hall effect (THE), we speculate that an antiskyrmion phase exists at finite fields and temperatures approaching the magnetic ordering temperature T_c that is highly favored by the crystalline structure.

II. SAMPLE PREPARATION AND EXPERIMENTAL METHODS

Single crystals of $\text{Cr}_{11}\text{Ge}_{19}$ were grown by a chemical vapor transport (CVT) method making use of the natural temperature gradient of a tube furnace. About 2.5 g of Cr and Ge powder were sealed in a quartz tube with a molar ratio of 45 : 55 [18]. About 70–100 mg iodine (2.2 mg/cm^3) was used as transfer agent. The temperature was maintained at 880°C at the deposition zone and 750°C at the source end. After 1-month growth, single crystals of $\text{Cr}_{11}\text{Ge}_{19}$ of average size $1 \times 1 \times 0.5 \text{ mm}$ were obtained. In addition to crystals of $\text{Cr}_{11}\text{Ge}_{19}$, the deposition zone contained single crystals of other phases such as CrGe and pure Ge. Crystals of $\text{Cr}_{11}\text{Ge}_8$

TABLE I. Single-crystal refinements for $\text{Cr}_{11}\text{Ge}_{19}$ at $296(2) \text{ K}$.

	Value
Refined formula	$\text{Cr}_{11}\text{Ge}_{19}$
Formula weight (g/mol)	1951.21
Space group; Z	$P4_1n2$; 4
a (Å)	5.801(3)
b (Å)	5.801(3)
c (Å)	52.38(3)
Volume (Å ³)	1762.7(18)
Extinction coefficient	0.00080(7)
θ range (deg)	0.777–33.046
No. of reflections; R_{int}	12029; 0.0377
No. of independent reflections	3218
No. of parameters	142
R_1 ; ωR_2 [$1 > 2\delta(1)$]	0.0531; 0.1389
Goodness of fit	1.286
Diffraction peak and hole ($e/\text{Å}^3$)	2.073; -3.111
Absolute structure parameter	0.5(1)

were obtained when the deposition zone was maintained at 1100°C .

$\text{Cr}_{11}\text{Ge}_{19}$ crystals grown via this method are typically in the shape of a flat-top pyramid as shown in Fig. 1(c). We measured the chemical composition of these crystals via energy-dispersive x-ray spectroscopy (EDX) spectra with the composition determined to be $\text{Cr}_{38.3 \pm 2.2}\text{Ge}_{61.7 \pm 2.7}$, well within the range expected for a Nowotny chimney ladder compound and in accordance with the previous reports [18,19]. The crystal structure and orientation are determined through single-crystal x-ray diffraction. The single-crystal refinements for $\text{Cr}_{11}\text{Ge}_{19}$ are summarized in Table I.

Temperature- and field-dependent dc magnetization and ac susceptibility measurements were performed on a Quantum Design (QD) Magnetic Property Measurement System (MPMS). No corrections for demagnetizing fields have been performed. The resistivity and Hall measurements were carried out in a QD Physical Property Measurement System (PPMS). Thin platinum wires were attached to polished surfaces of single crystals via conductive epoxy (Epo-Tek H20E) for charge transport measurements. Resistivity and Hall effect measurements were performed using standard four-terminal low-frequency ac techniques using a current of 20 mA at 17 Hz. Field reversal in the Hall measurements was used to compensate for any misalignment of the leads through subtraction of the symmetric part of the field response. The dimension of this crystal was about $1 \times 0.83 \times 0.093 \text{ mm}^3$, and the applied current density was $0.21 \times 10^7 \text{ A/m}^2$.

III. EXPERIMENTAL RESULTS AND DATA ANALYSIS

A. Magnetization and susceptibility

We first present the magnetic field, H , dependence of the magnetization M , with H parallel and perpendicular to the c axis at 50 K, in Fig. 2(a). The different saturation fields of M for $H \parallel c$ and $H \parallel ab$ indicate an easy-axis magnetic anisotropy along the c axis. The saturated magnetic moment is small, $\sim 0.6 \mu_B$, at 50 K and 5 T, consistent with previous reports [15,18–20]. In Fig. 2(b), we display a series of

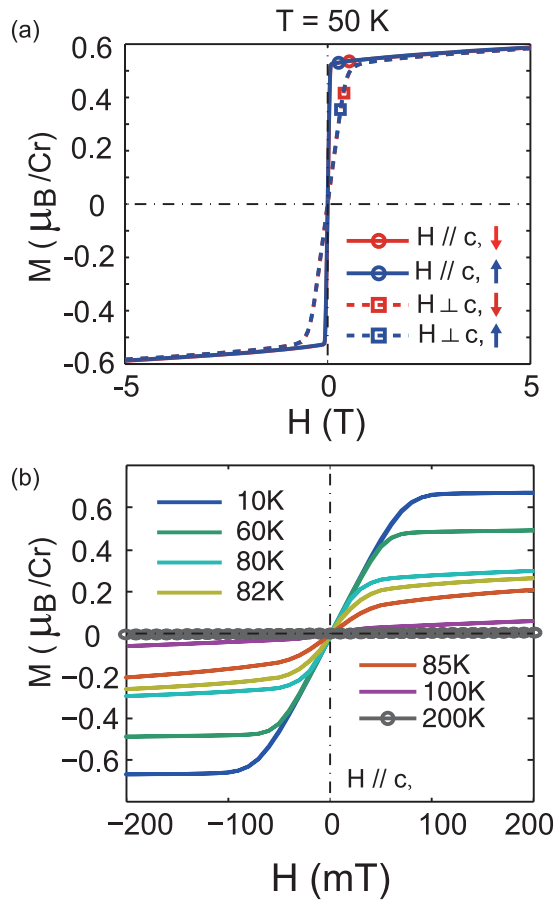


FIG. 2. Magnetization. (a) Field dependence, H , of the magnetization M . Solid (dashed) lines represent the case where the applied field is along (perpendicular to) the c axis. (b) Magnetization loops measured at a series of temperatures after field cooling at 5 T.

magnetization loops with $H \parallel c$ at a variety of temperatures after the same field-cooling (FC) process at 5 T. We do not observe any remnant magnetic moment at zero field or a ferromagnetic hysteresis outside of a small antihysteresis loop induced by trapped flux in the superconducting magnet [21,22], which is too small to be seen in Fig. 2(b). The absence of a remnant magnetic moment, along with the easy-axis anisotropy, implies that the macroscopic magnetization is completely compensated among regions with different spin orientations, which can be either a ferromagnetic ordering with very soft domainlike structure or a periodically modulated ordered state such as a long-period spin density wave or stripe domain order with chiral Bloch domain walls.

Figure 3(a) displays the dc magnetic susceptibility, M/H , along with the inverse susceptibility $1/\chi = H/M$ for $H = 0.01$ and 1 T along the c axis. The magnetic transition temperature T_c is 83 K. We notice that there is a small anomaly where the data deviate significantly from a simple Curie-Weiss (CW) form for $T < 110$ K as demonstrated in Fig. 3(b), where M/H is presented on a logarithmic scale. A fit of the Curie-Weiss formula is illustrated by the solid black curve. The effective magnetic moment determined from the best-fit CW form is about $2.7 \pm 0.3 \mu_B$. A comparison of this effective moment with the saturated magnetic moment found in the data of

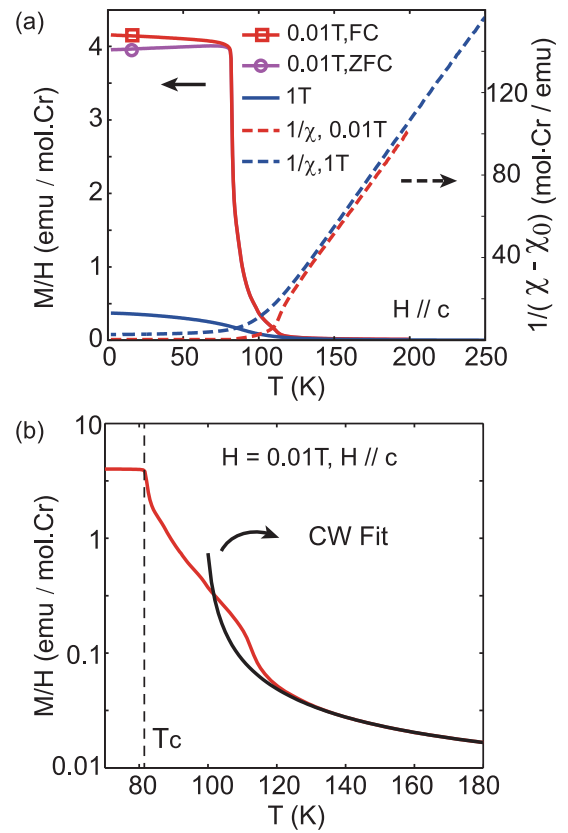


FIG. 3. (a) dc magnetization, M/H , and its inverse, $1/\chi$, at 0.01 and 1 T. (b) M/H at $H = 0.01$ T on the log scale. The black curve is a fit of the Curie-Weiss form to the data. ZFC, zero-field cooling.

Fig. 2 reveals a Rhodes-Wohlfarth ratio $\mu_{\text{eff}}/\mu_{\text{sat}} \sim 4.5$ revealing a weakly itinerant character. The Weiss temperature Θ_W is 100 ± 2 K, higher than T_c but substantially below the temperature where the anomaly in M/H is observed. In general, the Curie-Weiss law describes the magnetic instability of a thermally disordered spin system at a mean-field level, which is expected not to be accurate in proximity to T_c due to the existence of critical fluctuations. For ferromagnetic (FM) materials with critical fluctuations, M/H can diverge at temperatures exceeding Θ_W . However, there are also exceptions such as $\text{Sr}(\text{Co}_{1-x}\text{Ni}_x)_2\text{As}_2$ [23], where a helical magnetic order is established at a temperature below Θ_W in the presence of magnetic frustration. We argue that the anomaly at 110 K is unlikely to be due to a second phase as there are no Cr-Ge compounds with a magnetic transition temperature in this range. However, local defects can be induced by the relative sliding between the highly incommensurate Cr and Ge helices. It is possible that these defects promote a tendency for local enhancement of the magnetization as is observed in magnetic Griffiths phases discovered in disordered magnetic systems [24,25]. The range of ordering temperatures (70–90 K) reported for this compound is likely a result of small differences in stoichiometry between samples grown under different conditions [18–20], with the level of disorder strongly tied to these differences in stoichiometry.

To further characterize the magnetic properties of $\text{Cr}_{11}\text{Ge}_{19}$, we explored the temperature dependence of the

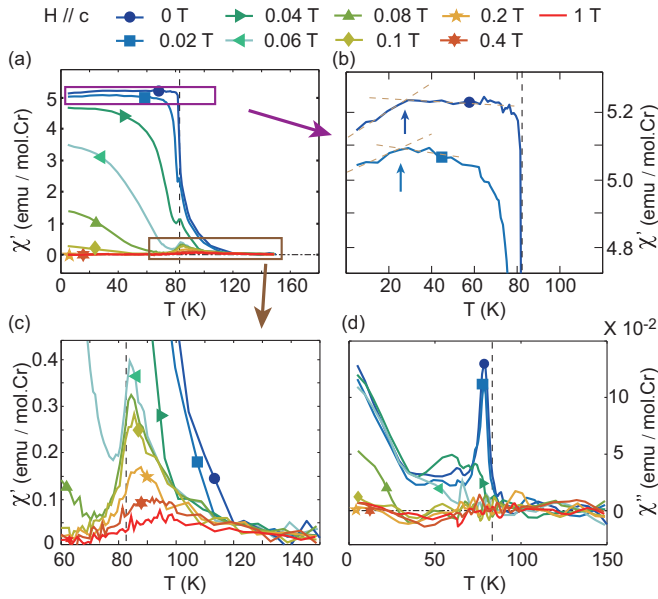


FIG. 4. Temperature and field dependence of the ac susceptibility. (a)–(c) Real part of the ac susceptibility χ' in Cr₁₁Ge₁₉ at magnetic fields H identified at the top of the figure. (b) and (c) are the magnification of the two regions enclosed by purple and brown rectangles in (a). (d) The corresponding imaginary part of the ac susceptibility χ'' of Cr₁₁Ge₁₉. The vertical dashed lines represent T_c at $H = 0$.

real, χ' , and imaginary, χ'' , parts of the ac susceptibility under a series of magnetic fields parallel to the c axis as shown in Figs. 4(a) and 4(d). In Fig. 4(a), χ' taken at zero field diverges as the temperature approaches T_c from above, and it exhibits a nearly constant value below T_c suggesting a strongly polarizable state. The principal maximum in χ' is suppressed and shifts to lower temperatures as the field increases, while a small peak remains near the zero-field T_c . This is similar to what was observed in FM AuFe [26], in which the principal maximum is associated with the motion of domain walls while the small peak around T_c is promoted by the applied field as shown in Fig. 4(c). While the magnitude of this peak is suppressed by the applied magnetic field, it is still observable up to 1 T, separating the nearly polarized FM (NPFM) state and the high-temperature paramagnetic (PM) phase. In Fig. 4(b), a small decrease in χ' is indicated by arrows below 30 K at 0 T and 20 mT. We associate these features with a change in, or stabilization of, the magnetic domains. On the other hand, χ'' in Fig. 4(d) displays a strong peak near T_c for $H < 40$ mT. An unusual enhancement of χ'' with cooling below 30 K at low H was also observed, consistent with a change in the structure and dynamics of magnetic domains in this temperature range. Both of these features disappear above 0.1 T, suggesting that they are associated with phases located in the low-field region. It is interesting to study the frequency dependence of the ac susceptibility to unveil the slow dynamics.

In Figs. 5(a) and 5(c), the field dependence of χ' and χ'' is presented at a series of temperatures. The magnitude of χ' at zero field is relatively unchanged below $T_c = 83$ K, in accordance with the temperature-dependent χ' in Fig. 4(a). As the field increases, χ' is gradually suppressed to zero in the NPFM

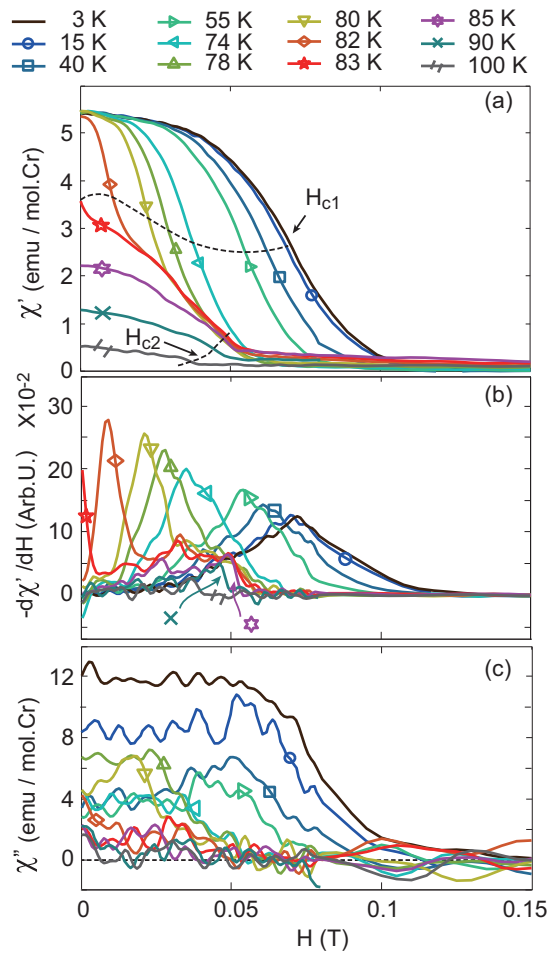


FIG. 5. Field dependence of the ac susceptibility. (a) Field dependence of χ' with the field along the c axis at temperatures T identified at the top of the figure. (b) The corresponding derivative $-d\chi'/dH$. The maximum defines the critical field, which is labeled as H_{c1} in (a). Note that a second peak appears around 0.05 T when the main peak shifts toward zero field as the temperatures increase. The second peak in $-d\chi'/dH$ leads to the broad feature of $\chi'(H)$ above T_c in (a). (c) The imaginary susceptibility χ'' as a function of the magnetic field at the corresponding temperatures.

state at $H > 0.1$ T and $T < T_c$. We define the critical field H_{c1} by the peaks in $-d\chi'/dH$ as shown in Fig. 5(b). From Fig. 5(b), it is clear that H_{c1} is reduced to zero as the temperature approaches T_c . By contrast, an extra contribution to $\chi'(H)$ appears for $H < 0.05$ T at temperatures close to T_c . Again, we define H_{c2} as the characteristic field from $-d\chi'/dH$ in Fig. 5(b). This additional contribution in χ' at small fields ($H < H_{c2}$) is responsible for the anomaly observed in the dc susceptibility at 0.01 T and above T_c [Fig. 3(b)].

In order to present a complete overview of the magnetic susceptibility of Cr₁₁Ge₁₉ as a function of temperature and magnetic field along the c axis, we display a H - T contour plot of χ' and χ'' in Figs. 6(a) and 6(b). χ' is shown on a log scale in Fig. 6(a) to highlight features with small magnitude. In Fig. 6(a), a red-colored ridge with high intensity is located between the NPFM phase and the high- T paramagnetic state and can be tracked back to T_c at zero field.

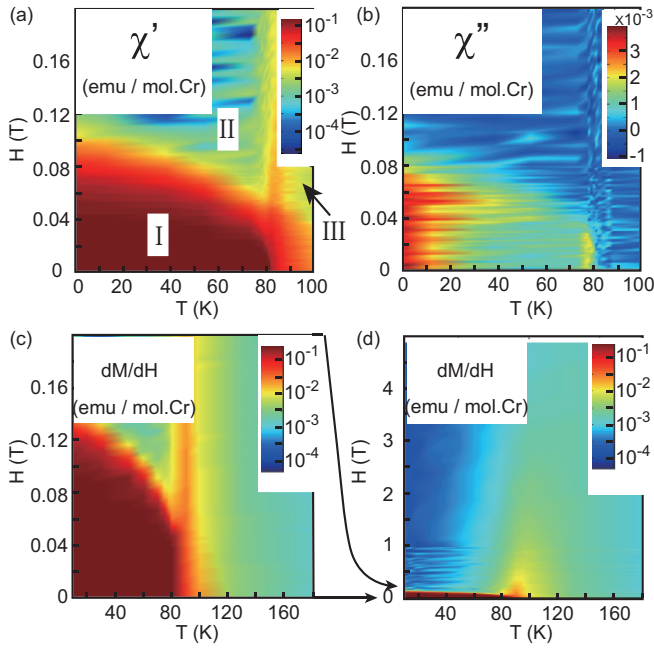


FIG. 6. ac and dc susceptibility. (a) and (b) Color plots of the real, χ' , and imaginary, χ'' , ac susceptibility as functions of magnetic field H and temperature T from the data in Fig. 5. (c) and (d) The dc susceptibility, dM/dH , of $\text{Cr}_{11}\text{Ge}_{19}$ shown in small and large field scales as a comparison.

This ridge corresponds to small peaks around T_c in $\chi'(T)$ in Fig. 4(c). Moreover, the large values (red area) at small fields appear to continue through the ridge at T_c , so that there is substantial intensity above T_c . Furthermore, it was found that the imaginary part of the ac susceptibility χ'' behaves differently above and below 30 K in the low-field region. In Figs. 6(c) and 6(d), the dc susceptibility, dM/dH , shares the same essential features as χ' . The red-colored ridge at low fields becomes diffuse as the field increases and but is still distinguishable up to 1 T [Fig. 6(d)].

In addition to the data presented above for fields oriented parallel to the c axis, we have also explored the magnetic response for fields along the ab plane. In Fig. 7, we display the temperature dependence of χ'_{ab} and χ''_{ab} of $\text{Cr}_{11}\text{Ge}_{19}$ at a series of magnetic fields. $\chi'(T)$ at zero field displays a continuous decrease as the temperature is reduced from T_c , unlike the plateau seen at zero field in Fig. 4(a). The differences seen here and in Fig. 4(a) for $H = 0$ are indicative of the intrinsic anisotropy of $\text{Cr}_{11}\text{Ge}_{19}$ as the only difference between these two measurements is the direction of the small ac magnetic fields. Moreover, the evolution of the principal maximum and a secondary peak around T_c is similar to that observed in χ' with H parallel to c . The imaginary part, χ''_{ab} , however, is featureless within the uncertainty of our measurements. In a previous report on polycrystals, a broad peak and a shoulder were observed under magnetic fields and were interpreted as a manifestation of both the itinerant and local moments [19]. With the consideration of both field parallel and field perpendicular to the c axis, our measurements on single crystal are consistent with the previous observation but suggest different origins.

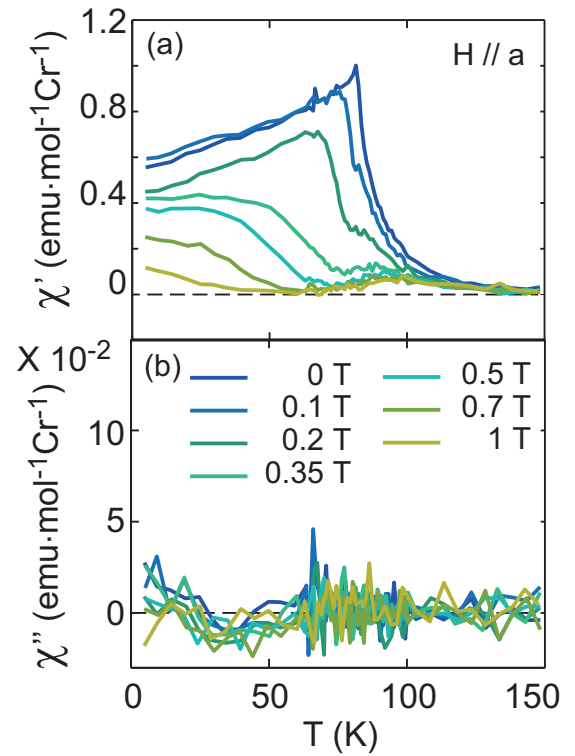


FIG. 7. ac susceptibility with field in the ab plane. (a) The temperature dependence of the real part of the ac susceptibility χ' under magnetic fields parallel to the a axis. (b) The corresponding imaginary part of the ac susceptibility χ'' as a function of temperature.

B. Charge transport measurements

In this section, we will present the results of transport measurements performed on the same single crystal of $\text{Cr}_{11}\text{Ge}_{19}$ with a focus on the topological Hall effect. The resistivity of $\text{Cr}_{11}\text{Ge}_{19}$ with current along the ab plane is measured at zero field as a function of temperature as shown in Fig. 8(a). The resistivity is reduced as the temperature decreases, indicating a metallic behavior. The residual-resistivity ratio (RRR), taken as the ratio of the resistivity at 300 K to that at 10 K, $\rho_{xx}(300\text{ K})/\rho_{xx}(10\text{ K})$, is about 19, with the resistivity continuing to decline significantly even for temperatures below 10 K. The derivative, $d\rho_{xx}/dT$, is also plotted as the blue curve in Fig. 8(a). A dramatic increase in $d\rho_{xx}/dT$ below the magnetic transition temperature T_c indicates a reduction in the magnetic fluctuations with ordering causing a decrease in the resistivity with cooling. A slight downturn in $d\rho_{xx}/dT$ was observed below 20 K, indicating the loss of a mechanism for carrier scattering at low temperatures. In Fig. 8(b), we present the electric conductivity σ as $1/\rho_{xx}$. The value of σ is less than $10^4 (\Omega\text{ cm})^{-1}$ above 50 K and quickly increases below this temperature.

Because the THE is a leading indicator for the existence of nontrivial spin textures, we measured the topological Hall resistivity ρ^T of $\text{Cr}_{11}\text{Ge}_{19}$ through a series of measurements of $M(H)$, Hall resistivity ρ_{xy} , and magnetoresistance (MR) on the same single crystal with the same field orientation along the c axis.

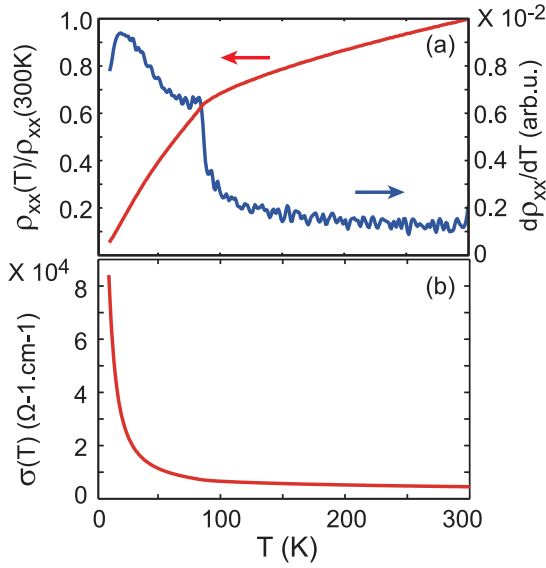


FIG. 8. Resistivity and conductivity. (a) The resistivity ρ_{xx} measured with the current in the ab plane. The blue curve is the derivative $d\rho_{xx}/dT$. (b) The corresponding electric conductivity, $\sigma = 1/\rho_{xx}$, as a function of the temperature.

In Fig. 9, we present the transverse magnetoresistance, $\Delta\rho_{xx}(H)/\rho_{xx}(0) = \frac{\rho_{xx}(H) - \rho_{xx}(0)}{\rho_{xx}(0)}$, with $I \perp c$ and $H \parallel c$ for $T < T_c$ [Figs. 9(a) and 9(b)] and $T > T_c$ [Figs. 9(c) and 9(d)]. A negative MR [27], which is characteristic of ferromagnetic materials, is observed, reflecting the suppression of electron-spin scattering by the applied magnetic field. We expand the low-field region of the magnetoresistance in Fig. 9(b) for $T < T_c$. It is clearly seen that the resistivity is nearly constant below H_{c1} and then quickly drops as the system enters into the NPFM phase. Although there is no magnetic order for $T > T_c$, a convex MR is still observed with a characteristic field illustrated by the dashed lines in Fig. 9(d). This characteristic field increases as the temperature increases. At higher magnetic field, a concave behavior of the MR is restored [Fig. 9(c)].

The temperature dependence of the MR is shown in Fig. 10, in which we plot $\Delta\rho_{xx}(H)/\rho_{xx}(0)$ as a function of temperature at $H = 0.5, 2,$ and 5 T. The local minimum of the MR around T_c indicates a significant contribution of spin fluctuations. We find a significant and unexpected enhancement of the negative MR below 50 K. This effect is particularly significant at high fields as demonstrated by the MR at 5 T in Fig. 10. Furthermore, a slight upturn of MR below 15 K is also observed, indicating either a subsidence of the mechanism causing the negative MR or an additional positive contribution at low T . These results are consistent with a previous observation [20].

In Fig. 11, we display M and ρ_{xy} of the same single crystal as a function of the field along the c axis for a series of temperatures. The Hall effect of magnetic materials is commonly written as [10,11]

$$\rho_{xy} = R_0 \mathbf{B} + S_A \rho_{xx}^2 \mathbf{M} + \rho^T. \quad (1)$$

in which ρ_{xx} is the longitudinal resistivity, R_0 and S_A are the normal and anomalous Hall coefficients, respectively, and \mathbf{B} represents the magnetic flux density. In this analysis we have

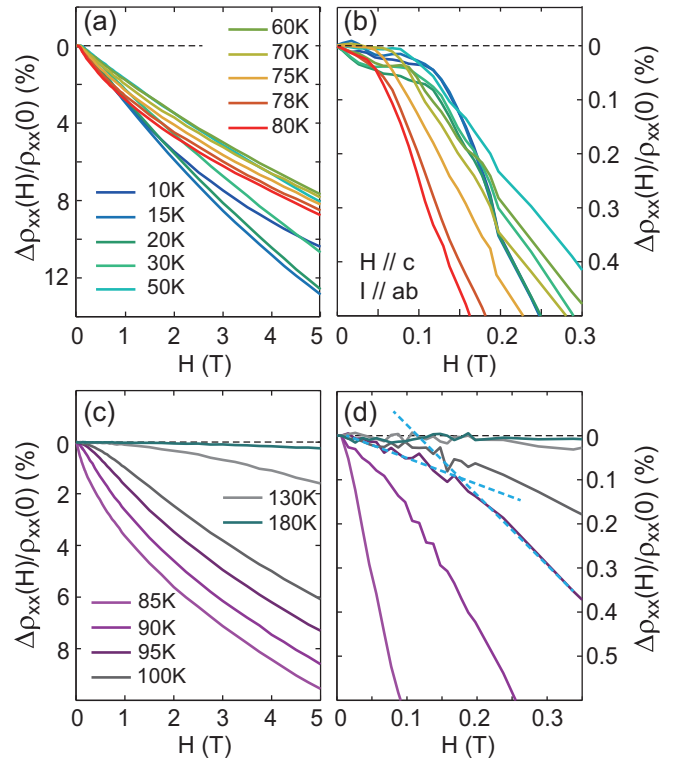


FIG. 9. Magnetoresistance, $\Delta\rho_{xx}(H)/\rho_{xx}(0)$, on a large and a small scale to highlight the regime of low field H for temperatures below T_c [(a) and (b)] and above T_c [(c) and (d)], respectively. The field is applied along the c axis, and the current is in the ab plane. ρ_{xx} is defined as the resistivity.

ignored contributions from skew scattering to the anomalous Hall resistivity, which is linear in ρ_{xx} , since it is expected to be insignificant [28] when σ_{xx} is smaller than $10^6 (\Omega \text{ cm})^{-1}$, as suggested in Fig. 8(b). In order to estimate the coefficients R_0 and S_A , we plot $\frac{\rho_{xy}}{H}$ vs $\frac{\rho_{xx}^2 M}{H}$ in Fig. 12(a). In the high field range ($H > 1$ T), where any contribution from a topological contribution to the Hall effect will likely be very small, the Hall resistivity is expected to obey the standard form of $\frac{\rho_{xy}}{H}$

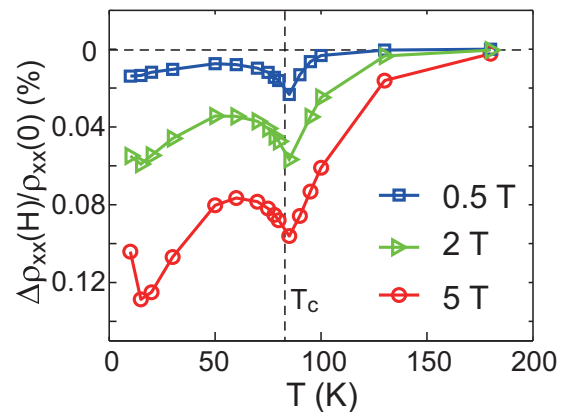


FIG. 10. Temperature dependence of the magnetoresistance, $\rho_{xx}(H, T)/\rho_{xx}(0, T)$, at magnetic fields $H = 0.5, 2,$ and 5 T. The vertical dashed line represents T_c at zero field.

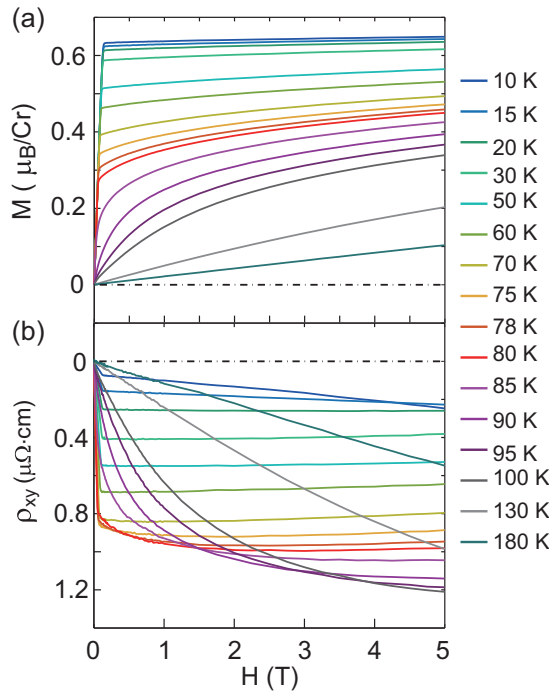


FIG. 11. Magnetization M and Hall resistivity ρ_{xy} as a function of magnetic field H at the series of temperatures denoted on the right.

$= R_0 + S_A \frac{\rho_{xy}^2 M}{H}$ allowing an accurate determination of R_0 and S_A . This form is represented in Fig. 12(a) as solid lines. It is clear from the figure that the data are largely described by this form. However, substantial deviation is apparent at lower fields, between 0.2 and 1 T, such that a substantial mismatch was observed between the linear form and the data. The values of R_0 and S_A that result from the fitting procedure are shown in Fig. 12(b).

With R_0 and S_A determined in this manner, we have calculated the Hall signal expected over the entire range of fields measured using Eq. (1) without the topological Hall term as presented for two temperatures in Fig. 13. The difference is ascribed to the topological Hall term, ρ^T . To establish the repeatability of our determination of the topological Hall term, we performed the same sequence of measurements on a second crystal of $\text{Cr}_{11}\text{Ge}_{19}$ having a somewhat different $T_c = 74$ K. The results are largely similar, including reproducing the values of R_0 and S_A , except that the positive ρ^T at low fields and low temperature ($H < T_{c1}$, $T < T_c$) as denoted by the red arrow in Fig. 13(b) is absent in sample 2. We argue that the different thickness (0.18 mm) and current densities ($0.06 \times 10^7 \text{ A/m}^2$) may be responsible for the difference in ρ^T at temperatures below T_c at low fields.

In Fig. 14, we plot the resultant ρ^T for sample 1 as a function of field in large ($0 < H < 5$ T) [Fig. 14(a)] and small ($0 < H < 0.4$ T) [Fig. 14(b)] field scales. We find that in spite of a complicated field and temperature dependence, the ρ^T display a clear response to the critical field H_{c1} in Fig. 14(b), implying a change in the underlying spin texture. To illustrate the evolution of ρ^T with the field and temperature, we present a H - T color contour plot of ρ^T in Fig. 15(a). The red (blue) color corresponds to values of ρ^T that are positive (negative).

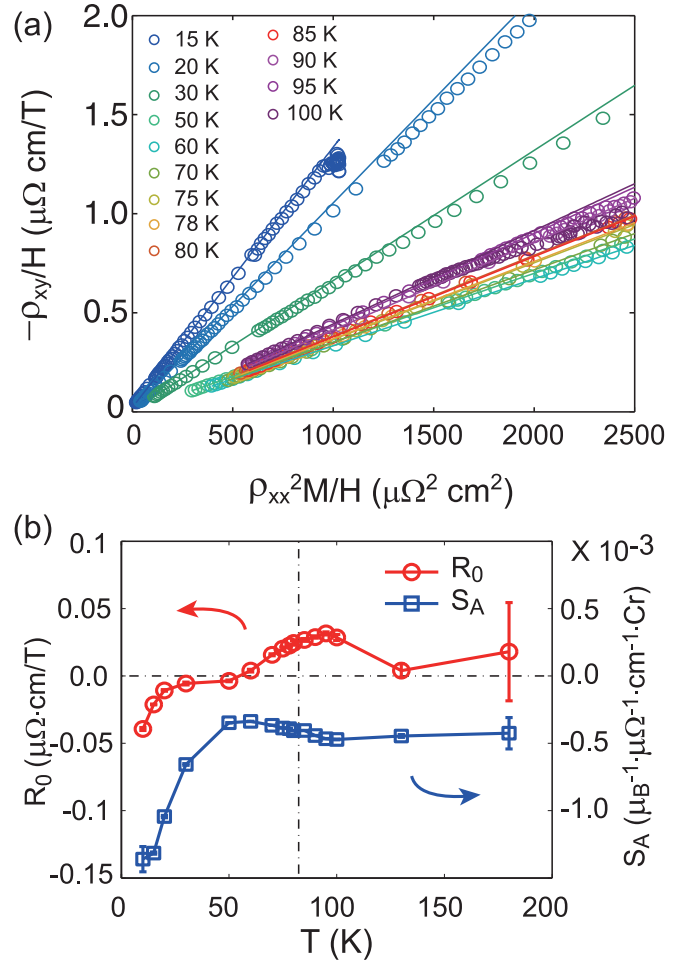


FIG. 12. (a) $\frac{\rho_{xy}}{H}$ vs $\frac{\rho_{xx}^2 M}{H}$ curves for various temperatures. Solid lines are the fits of a linear form to the data at $H > 1$ T. (b) The normal, R_0 , and anomalous, S_A , Hall coefficients obtained from the fits demonstrated in (a). The error bars represent errors of the fit.

Figure 15(b) displays the same data on a magnified field scale to highlight the low-field region. The white lines are the phase boundaries separating the polarizable low-field, NPFM, and high- T PM phases. Apparently, ρ^T changes sign near the boundaries of the magnetic phases, as well as displaying a positive value below 30 K where the negative contribution to the MR grows, and the values of R_0 and S_A display significant and unexpected temperature dependence. This can be further confirmed in the T dependence of ρ^T as shown in Fig. 15(c), in which $\rho^T(T)$ is presented for several fields and where ρ^T is observed to cross the x axis twice in the temperature range $30 \text{ K} < T < 100 \text{ K}$ for $H = 0.05, 0.2, 0.4,$ and 1 T. Furthermore, the maximum of $\rho^T(T)$ found just above T_c moves towards high temperatures as the field increases, following the evolution of T_c determined by the peak of the ac susceptibility, as indicated by the arrows.

In Fig. 16, we plot a schematic phase diagram as a summary of our magnetic and charge transport measurements. Regions I, II, and III are the three main phases, referring to the polarizable low-field phase, the NPFM phase, and the high- T PM states, respectively. Region II is further split into regions II-R and II-L. In the latter, the Hall constants R_0 and

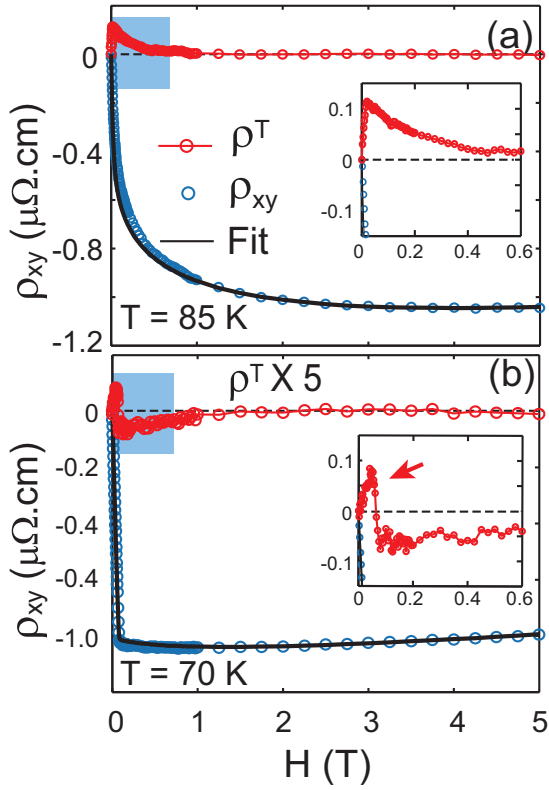


FIG. 13. Hall resistivity ρ_{xy} (blue) and the best-fit result of $\frac{\rho_{xy}}{H} = R_0 + S_A \frac{\rho_{xy}^2 M}{H}$ to these data at high fields. The difference, plotted as red circles, is interpreted as the THE, ρ^T . Insets: Magnification of the regions indicated by the blue shading.

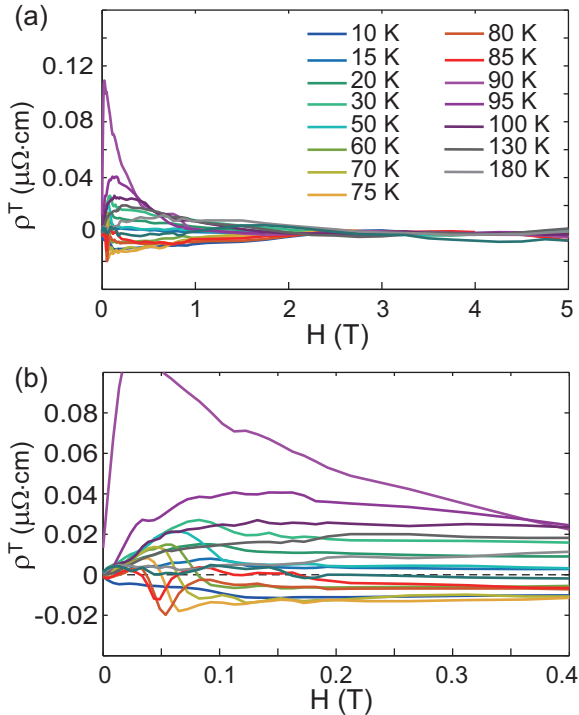


FIG. 14. Topological Hall resistivity. (a) The estimated topological Hall resistivity ρ^T at different temperatures. (b) Magnification of the low-field region in (a).

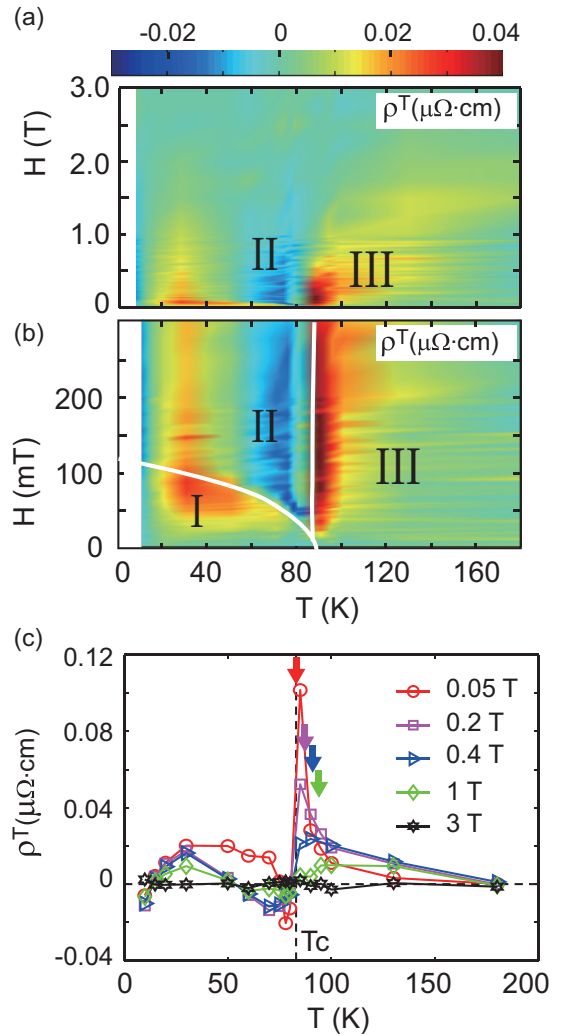


FIG. 15. Temperature and field dependence of the topological Hall resistivity. (a) Magnetic field H and temperature T dependence of the topological Hall resistivity ρ^T . (b) ρ^T shown on a smaller field scale to emphasize the features at low fields. The white curves are the boundaries separating the polarizable low-field, NPFM state, and high- T_c PM phases. (c) T dependence of ρ^T at a few selected fields. The arrows represent the locations where χ' displays a maximum at the corresponding fields.

S_A and the MR display significant changes, suggesting that there may be changes to the underlying electronic structure. In region I below 30 K, the ac magnetic susceptibility is slightly reduced, while a large enhancement of χ'' is observed. It remains an open question whether these observations signal a new phase. However, we denote this as region V to leave open this possibility and to speculate that a magnetic texture may be forming in this region. In addition, we identify an additional phase as region IV just above T_c and below H_{c2} where χ' is significant.

IV. DISCUSSION AND CONCLUSION

To place the phase diagram of Fig. 16 in context, it is helpful to recall previous studies on two-dimensional dipolar ferromagnets [29]. In FM films with an easy-axis anisotropy,

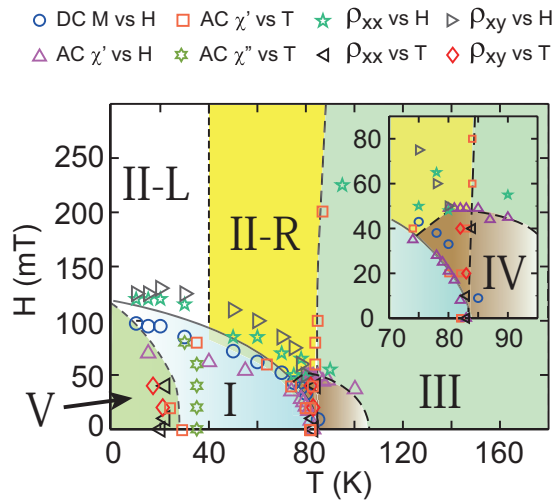


FIG. 16. Schematic of the magnetic phase diagram determined from our magnetic and charge transport measurements. Inset: Magnification of the area near the critical point. The symbols represent the different measurement techniques listed at the top.

it is known that the magnetic dipolar interaction drives the ground state into stripe ordered domains. When a magnetic field is applied, these magnetic stripes break into an intermediate phase of magnetic bubbles, which ultimately dissolve into the field-polarized FM state under larger applied fields [30,31]. In $\text{Cr}_{11}\text{Ge}_{19}$, the existence of easy-axis spin anisotropy is demonstrated in Fig. 2(a). While the stripe domains have not been observed, broken stripes or elongated bubbles are indeed found in LTEM images of thin lamellae at 6 K and zero field [15]. It is plausible that the ground state of $\text{Cr}_{11}\text{Ge}_{19}$ is a stripe order with a zero remnant magnetization as mentioned above. The idea that the magnetic order becomes more stripelike at low temperatures corresponds well with the decreased χ' at low field with a corresponding increase in χ'' below 30 K. With these considerations, we speculate that region V in Fig. 16 is related to the stripe-ordered domain phase.

Conversely, a disordered magnetic bubble state may be realized in region I. As a special kind of magnetic bubble, biskyrmions [Fig. 1(d)] are formed from a pair of skyrmions with opposite helicities via attractive interactions. Each skyrmion carries a topological charge (scalar spin chirality) defined as $Q = \frac{1}{4\pi} \int d^2r (\partial_x \mathbf{m} \times \partial_y \mathbf{m}) \cdot \mathbf{m}$, where \mathbf{m} is a unit vector pointing in the direction of the magnetization. As a spin-polarized electron passes through the spin texture of a skyrmion, it experiences an emergent fictitious magnetic field causing a finite THE. The direction of the fictitious magnetic field is directly related to the sign of Q , which distinguishes skyrmions (positive) and antiskyrmions (negative). The THE from biskyrmions has been observed as a function of field and temperature in centrosymmetric MnNiGa and MnPdGa systems [10,11] and is also anticipated in $\text{Cr}_{11}\text{Ge}_{19}$. The positive THE that we observe in region I suggests that biskyrmions may be present. However, the temperature range of region I does not agree with the observation in the LTEM images, in which biskyrmions were seen at 6 K. We speculate that this may be due to the small thickness of the LTEM sample, which

allows dipolar fields to stabilize these skyrmion features [32], whereas in our bulk crystalline samples, the effect of these fields is expected to be smaller. Furthermore, since the THE resistivity relies on the fictitious effective field B_{eff} , the local spin polarization of the charge carriers P , and the normal Hall coefficient R_0 , we compared these values for both the MnNiGa system and $\text{Cr}_{11}\text{Ge}_{19}$, finding comparable values of ρ^T . We conclude that there is a distinct possibility of a biskyrmion phase in $\text{Cr}_{11}\text{Ge}_{19}$ for sample 1 in the region characterized by a positive ρ^T . In addition, the decreased THE in region V suggests that for bulk samples the magnetic bubble phase transitions to a fully formed magnetic stripe phase at low temperatures. Therefore we attribute region I to the biskyrmion state in $\text{Cr}_{11}\text{Ge}_{19}$.

Next, we turn our attention to region II-R at intermediate temperatures and magnetic fields. Across the boundary between regions I and II-R, we can clearly see a sign change of ρ^T from positive in region I to negative in region II-R at temperatures $60 \text{ K} < T < 80 \text{ K}$. The sign reversal is sharp and deep for temperatures within 5 K of T_c . Sign reversal in ρ^T near T_c was previously reported in MnGe [33] and recently explained as the competition between the THE from the skyrmion lattice and skew scattering from chiral fluctuations [34]. A similar phenomenon observed here suggests that this mechanism may also apply as we have speculated that biskyrmions may be present and where LTEM images indicate biskyrmions in thin samples. We note that at 80 K, there are distinct contributions to the negative THE at low and high fields suggesting different origins.

In noncentrosymmetric magnetic materials with spin-orbital coupling, the Dzyaloshinskii-Moriya (DM) interaction in the absence of inversion symmetry is responsible for many interesting magnetic configurations and slow dynamics. In $\text{Cr}_{11}\text{Ge}_{19}$, while the spin dipolar interaction plays a significant role in the formation of biskyrmions at low temperatures, it is expected to be weak or even absent in the vicinity of T_c due to the fast spin fluctuations. Near T_c , it is anticipated that the anisotropic DM interaction supported by the D_{2d} crystal symmetry may impose a strong effect on the spin dynamics and transport properties. In Figs. 15(a)–15(c), we observed a large positive ρ^T around T_c which persists deep into the paramagnetic phase in region III. This strongly suggests that the positive large ρ^T is induced by thermal fluctuations. Recently, it was proposed that nonzero spin chirality arises as a consequence of the melting of ferromagnetic order by thermal fluctuations in the presence of DM interaction. This mechanism was observed in two different ferromagnetic ultrathin films of SrRuO_3 and V-doped Sb_2Te_3 where the temperature dependence of ρ^T shows a maximum at T_c [35]. Our data in Fig. 15(c) agree with this proposition, and the peak of ρ^T follows the boundary between the NPFM and PM phases, which is derived from the ac susceptibility and marked by the arrows. We note that the evolution between the field-polarized and PM phases is a crossover instead of a transition under finite magnetic fields.

The application of an external magnetic field explicitly breaks time-reversal symmetry of the zero-field Hamiltonian. Thus the transition between FM and PM phases in a FM material under a magnetic field does not involve symmetry breaking. Instead, the order parameter is smeared as a

crossover, much like a gas-liquid phase crossover at high pressure rather than a second-order phase transition. As the system goes from finite fields to zero field at T_c , it enters into the critical region filled by strong fluctuations. In spite of the absence of symmetry breaking, the spin chirality fluctuations in the presence of DM interaction introduce a finite topological charge density and separate the NPFM and PM states. We notice that such spin chirality fluctuations persist up to 1 T, above which the NPFM and PM phases are continuously connected.

Furthermore, unlike the isotropic DM interaction in MnSi [5,6], the anisotropic DM interaction in $\text{Cr}_{11}\text{Ge}_{19}$ favors the spin texture of antiskyrmions, which we speculate is the cause of the robustly negative ρ^T that we discover in both samples measured. In Figs. 15(a) and 15(b), the broad blue area with negative THE suggests that it is not an ordinary FM phase and instead contains topologically nontrivial spin textures. Specifically, the opposite sign of THE in regions I and II-R represents different topological charges and implies that antiskyrmions may exist in region II-R for finite fields close to T_c where a negative THE is observed. We note that the positive THE found in region II-L is dependent on details of our data analysis and differs for the two samples investigated leading to some ambiguity in the THE in this region of the phase diagram [36–38].

The DM interaction relies on the electronic structure [39], which may evolve with temperature below T_c as suggested by the Hall coefficients (both R_0 and S_A show a temperature dependence) in Fig. 12(b). Interestingly, we also notice that there is a broad maximum R_0 around T_c in Fig. 12(b), and this may suggest that the Fermi surfaces and low-energy electronic structure [40] are coupled with the critical fluctuations [Fig. 10], which may tune the strength of DM interaction in $\text{Cr}_{11}\text{Ge}_{19}$. On the other hand, the magnetic dipolar interaction is long-range in nature and can be screened by fast magnetic fluctuations at temperatures approaching T_c . These two factors lead to the dominance of the DM interaction around T_c and a greater importance of dipolar interactions at low temperatures. Therefore $\text{Cr}_{11}\text{Ge}_{19}$ provides an ideal platform to investigate the competition among the dipolar interaction, DM interaction, and magnetic anisotropy as well as the consequences on the underlying spin textures. Further investigation, such as small-angle neutron-scattering measurements and a thorough exploration of LTEM images, is required to confirm the existence of the purported antiskyrmion phase in $\text{Cr}_{11}\text{Ge}_{19}$.

Alternatively, the negative THE in region II-R may also be interpreted as changing character of the dominant charge carriers [41] from electronlike to holelike, as suggested by the change in sign of R_0 in Fig. 12(b). However, this cannot explain the sign change between regions II and III. It is also unlikely that biskyrmions survive in region II above H_{c1} . Instead, we suggest that $\text{Cr}_{11}\text{Ge}_{19}$ is a nearly compensated metal [42,43] in which the change in sign of R_0 can be attributed to a change in the relative scattering rates for electrons and holes.

Finally, the magnetic behavior near the FM critical point in $\text{Cr}_{11}\text{Ge}_{19}$ is very interesting. In Fig. 16, region IV as magni-

fied in the inset corresponds to a region of enhanced magnetic susceptibility and has a boundary determined by H_{c2} and the temperature of the anomaly T_{ano} . The enhanced magnetic susceptibility in this region is likely not due to simple enhanced critical fluctuations which are responsible for the ridgelike enhancement evident in Fig. 6. Instead, region IV is more likely a natural extension of the highly polarizable FM domains in region I. This suggests that spin clusters which fluctuate substantially in space and time persist well above the melting point, T_c , of the magnetic order. The slow dynamics of these spin clusters may account for the temperature dependence of the magnetic susceptibility above T_c at low fields, much like that observed in Griffiths phase systems [24,25]. Recently, the hierarchy of three interactions in MnSi was considered with the weakest being the cubic anisotropy. Here, the hierarchy of interactions leads to an unusual critical regime known as a Brazovskii transition, a fluctuation-induced, weakly first-order, phase transition [44,45]. $\text{Cr}_{11}\text{Ge}_{19}$ clearly does not fit this description because of the very different crystal symmetry. Instead, region IV in the phase diagram of Fig. 16 may be the result of a more complex critical regime that reflects the complex interactions present in this system. These interactions include the increasing importance of the uniaxial anisotropy with cooling and an antisymmetric DM interaction which prefers an alternating chirality.

In summary, we have carried out a series of magnetic and charge transport measurements on single crystals of $\text{Cr}_{11}\text{Ge}_{19}$ unveiling a rich phase diagram. A set of interesting phases is postulated from the results of measurements of the ac susceptibility and the THE adding to the recently discovered biskyrmion phase in this material. A second topological nontrivial phase is postulated at temperatures approaching T_c which we believe may be an antiskyrmion phase consistent with the crystalline symmetry. In addition, the magnetic susceptibility at low fields is significantly enhanced above T_c , implying a cluster or disordered phase likely due to the anisotropy, the crystalline disorder, and the DM interaction, in contrast with that found in MnSi from the weak cubic anisotropy. Considering the likely difference in the temperature dependencies of the DM interaction and the magnetic dipolar interaction, we argue that a transition between the biskyrmion state at low temperature and an antiskyrmion state near T_c may be realized in $\text{Cr}_{11}\text{Ge}_{19}$. This is reminiscent of LTEM images of $\text{Mn}_{1.4}\text{Pt}_{0.9}\text{Pd}_{0.1}\text{Sn}$ [13,14], correlating the sign change of the THE with the change from biskyrmion to antiskyrmion phase.

ACKNOWLEDGMENTS

Y.L. is grateful to D. L. Gong, L. Y. Xing, and J. H. Chen for the assistance in measurements and thanks R. Y. Jin and Z. T. Wang for helpful discussions. We acknowledge D. M. Cao, Y. Mu, and X. C. Wu at the Shared Instrumentation Facility (SIF), LSU, for chemical analysis. This project is supported by the U.S. Department of Energy under EPSCoR Grant No. DESC0012432 with additional support from the Louisiana Board of Regents.

- [1] S. Mühlbauer, B. Binz, F. Jonietz, C. Pfleiderer, A. Rosch, A. Neubauer, R. Georgii, and P. Böni, *Science* **323**, 915 (2009).
- [2] S. Heinze, K. Von Bergmann, M. Menzel, J. Brede, A. Kubetzka, R. Wiesendanger, G. Bihlmayer, and S. Blügel, *Nat. Phys.* **7**, 713 (2011).
- [3] S. Seki, X. Z. Yu, S. Ishiwata, and Y. Tokura, *Science* **336**, 198 (2012).
- [4] X. Zhang, J. Xia, Y. Zhou, X. Liu, H. Zhang, and M. Ezawa, *Nat. Commun.* **8**, 1717 (2017).
- [5] N. Nagaosa and Y. Tokura, *Nat. Nanotechnol.* **8**, 899 (2013).
- [6] C. Dhital, L. DeBeer-Schmitt, Q. Zhang, W. Xie, D. P. Young, and J. F. DiTusa, *Phys. Rev. B* **96**, 214425 (2017).
- [7] A. K. Nayak, V. Kumar, T. Ma, P. Werner, E. Pippel, R. Sahoo, F. Damay, U. K. Rößler, C. Felser, and S. S. P. Parken, *Nature (London)* **548**, 561 (2017).
- [8] S. Huang, C. Zhou, G. Chen, H. Shen, A. K. Schmid, K. Liu, and Y. Wu, *Phys. Rev. B* **96**, 144412 (2017).
- [9] L. Peng, Y. Zhang, W. Wang, M. He, L. Li, B. Ding, J. Li, Y. Sun, X.-G. Zhang, J. Cai, S. Wang, G. Wu, and B. Shen, *Nano Lett.* **17**, 7075 (2017).
- [10] W. Wang, Y. Zhang, G. Xu, L. Peng, B. Ding, Y. Wang, Z. Hou, X. Zhang, X. Li, E. Liu, S. Wang, J. Cai, F. Wang, J. Li, F. Hu, G. Wu, B. Shen, and X.-X. Zhang, *Adv. Mater.* **32**, 6887 (2016).
- [11] X. Xiao, L. Peng, X. Zhao, Y. Zhang, Y. Dai, J. Guo, M. Tong, J. Li, B. Li, W. Liu, J. Cai, B. Shen, and Z. Zhang, *Appl. Phys. Lett.* **114**, 142404 (2019).
- [12] X. Li, S. Zhang, H. Li, D. A. Venero, J. S. White, R. Cubitt, Q. Huang, J. Chen, L. He, G. van der Laan, W. Wang, T. Hesjedal, and F. Wang, *Adv. Mater. (Weinheim)* **31**, 1900264 (2019).
- [13] L. Peng, R. Takagi, W. Koshibae, K. Shibata, K. Nakajima, T.-h. Arima, N. Nagaosa, S. Seki, X. Yu, and Y. Tokura, *Nat. Nanotechnol.* **15**, 181 (2020).
- [14] J. Jena, B. Göbel, T. Ma, V. Kumar, R. Saha, I. Mertig, C. Felser, and S. S. P. Parkin, *Nat. Commun.* **11**, 1115 (2020).
- [15] R. Takagi, X. Z. Yu, J. S. White, K. Shibata, Y. Kaneko, G. Tatara, H. M. Rønnow, Y. Tokura, and S. Seki, *Phys. Rev. Lett.* **120**, 037203 (2018).
- [16] D. C. Fredrickson, S. Lee, and R. Hoffmann, *Inorg. Chem.* **43**, 6159 (2004).
- [17] R. Castillo, W. Schnelle, M. Bobnar, R. Cardoso-Gil, U. Schwarz, and Y. Grin, *Z. Anorg. Allg. Chem.* **646**, 256 (2020).
- [18] H. Han, L. Zhang, X. Zhu, H. Du, M. Ge, L. Ling, L. Pi, C. Zhang, and Y. Zhang, *Sci. Rep.* **6**, 39338 (2016).
- [19] N. J. Ghimire, M. A. McGuire, D. S. Parker, B. C. Sales, J.-Q. Yan, V. Keppens, M. Koehler, R. M. Latture, and D. Mandrus, *Phys. Rev. B* **85**, 224405 (2012).
- [20] N. Jiang, Y. Nii, R. Ishii, Z. Hiroi, and Y. Onose, *Phys. Rev. B* **96**, 144435 (2017).
- [21] M. Buchner, K. Höfler, B. Henne, V. Ney, and A. Ney, *J. Appl. Phys. (Melville, NY)* **124**, 161101 (2018).
- [22] M. Sawicki, W. Stefanowicz, and A. Ney, *Semicond. Sci. Technol.* **26**, 064006 (2011).
- [23] Y. Li, Z. Liu, Z. Xu, Y. Song, Y. Huang, D. Shen, N. Ma, A. Li, S. Chi, M. Frontzek, H. Cao, Q. Huang, W. Wang, Y. Xie, R. Zhang, Y. Rong, W. A. Shelton, D. Young, J. F. DiTusa, and P. Dai, *Phys. Rev. B* **100**, 094446 (2019).
- [24] S. Guo, D. P. Young, R. T. Macaluso, D. A. Browne, N. L. Henderson, J. Y. Chan, L. L. Henry, and J. F. DiTusa, *Phys. Rev. Lett.* **100**, 017209 (2008).
- [25] M. B. Salamon, P. Lin, and S. H. Chun, *Phys. Rev. Lett.* **88**, 197203 (2002).
- [26] I. Maartense and G. Williams, *Phys. Rev. B* **17**, 377 (1978).
- [27] H. Yamada and S. Takada, *Prog. Theor. Phys.* **48**, 1828 (1972).
- [28] N. Nagaosa, J. Sinova, S. Onoda, A. H. MacDonald, and N. P. Ong, *Rev. Mod. Phys.* **82**, 1539 (2010).
- [29] K. De'bell, A. B. Maclsaac, and J. P. Whitehead, *Rev. Mod. Phys.* **72**, 225 (2000).
- [30] R. Díaz-Méndez and R. Mulet, *Phys. Rev. B* **81**, 184420 (2010).
- [31] T. Garel and S. Doniach, *Phys. Rev. B* **26**, 325 (1982).
- [32] X. Z. Yu, N. Kanazawa, Y. Onose, K. Kimoto, W. Z. Zhang, S. Ishiwata, Y. Matsui, and Y. Tokura, *Nat. Mater.* **10**, 106 (2011).
- [33] N. Kanazawa, Y. Onose, T. Arima, D. Okuyama, K. Ohoyama, S. Wakimoto, K. Kakurai, S. Ishiwata, and Y. Tokura, *Phys. Rev. Lett.* **106**, 156603 (2011).
- [34] H. Ishizuka and N. Nagaosa, *Sci. Adv.* **4**, eaap9962 (2018).
- [35] W. Wang, M. W. Daniels, Z. Liao, Y. Zhao, J. Wang, G. Koster, G. Rijinders, C.-Z. Chang, D. Xiao, and W. Wu, *Nat. Mater.* **18**, 1054 (2019).
- [36] S.-Y. Yang, Y. Wang, B. R. Ortiz, D. Liu, J. Gayles, E. Derunova, R. Gonzalez-Hernandez, L. Šmejkal, Y. Chen, S. S. P. Parkin, S. D. Wilson, E. S. Toberer, T. McQueen, and M. N. Ali, *Sci. Adv.* **31**, eabb6003 (2020).
- [37] N. Kanazawa, A. Kitaori, J. S. White, V. Ukleev, H. M. Rønnow, A. Tsukazaki, M. Ichikawa, M. Kawasaki, and Y. Tokura, *Phys. Rev. Lett.* **125**, 137202 (2020).
- [38] D. Hou, G. Su, Y. Tian, X. Jin, S. A. Yang, and Q. Niu, *Phys. Rev. Lett.* **114**, 217203 (2015).
- [39] T. Koretsune, N. Nagaosa, and R. Arita, *Sci. Rep.* **5**, 13302 (2015).
- [40] P. Pécheur, G. Toussaint, H. Kenzari, B. Malaman, and R. Welter, *J. Alloys Compd.* **262-263**, 363 (1997).
- [41] D. LeBoeuf, N. Doiron-Leyraud, J. Levallois, R. Daou, J.-B. Bonnemaison, N. E. Hussey, L. Balicas, B. J. Ramshaw, R. Liang, D. A. Bonn, W. N. Hardy, S. Adachi, C. Proust, and L. Taillefer, *Nature (London)* **450**, 533 (2007).
- [42] N. W. Ashcroft, *Phys. Kondens. Mater.* **9**, 45 (1969).
- [43] M. Zingl, J. Mravlje, M. Aichhorn, O. Parcollet, and A. Georges, *npj Quantum Mater.* **4**, 35 (2019).
- [44] M. Janoschek, M. Garst, A. Bauer, P. Krautscheid, R. Georgii, P. Böni, and C. Pfleiderer, *Phys. Rev. B* **87**, 134407 (2013).
- [45] J. D. Bocralsy, R. F. Need, R. Seshadri, and S. D. Wilson, *Phys. Rev. B* **97**, 100404(R) (2018).